# Three-Dimensional X-Ray Fourier Transform Holography: The Bragg Case

V. Chamard,[1,*] J. Stangl,[2] G. Carbone,[3] A. Diaz,[3,†] G. Chen,[2] C. Alfonso,[1] C. Mocuta,[3,‡] and T. H. Metzger[3]

[1]*IM2NP, CNRS, Aix-Marseille Université, avenue Escadrille Normandie Niemen, F-13397 Marseille Cedex 20, France*

[2]*Institute of Semiconductor and Solid State Physics, Johannes Kepler Universität, A-4040 Linz, Austria*

[3]*European Synchrotron Radiation Facility, BP220, F-38043 Grenoble, France*

(Received 18 January 2010; published 19 April 2010)

A novel approach to determine the structure of nanoscale crystals in three dimensions is proposed by the use of coherent x-ray Fourier transform holography in Bragg geometry. The full internal description is directly obtained by a single Fourier transform of the 3D intensity hologram. Together with the morphology, Bragg geometry gives access to the 3D displacement field within the crystal. This result opens great possibilities for the investigation of strain fields inside nanocrystals in a simple way.

DOI: 10.1103/PhysRevLett.104.165501 PACS numbers: 61.05.C−, 42.30.Rx, 61.46.Hk, 68.37.Yz

Hard x rays are one of the most applied probes in material science [1]. Their weak interaction with matter allows for a nondestructive *in situ* investigation, making x-ray techniques complementary to invasive electron microscopy methods. They are particularly relevant in nanosciences [2], where detailed knowledge of the internal structure on the nanoscale is fundamental to understand and monitor the nanostructure's physical properties [3]. However, the impossibility to measure the phase of the diffracted beams, known as the ''phase problem,'' is a strong limitation. Therefore, the analysis of the diffraction patterns typically relies on model-dependent approaches.

Lensless microscopies provide an elegant solution to the phase problem. These rapidly developing imaging techniques are based on the digital retrieval of the phase from the object's coherently diffracted intensity patterns. They require coherent x-ray beams provided by highly brilliant third generation synchrotron sources. The inversion is obtained by iterative algorithms [4–7]. However, the inversion of the intensity patterns is highly demanding in terms of time and computational power. In comparison, Fourier transform holography (FTH) is in essence extremely simple and fast: The sample image is directly obtained by a *single* inverse Fourier transform of the far-field *intensity* pattern. Contrarily to iterative algorithms, where the convergence is obtained within hours, the FTH inversion is obtained in a few seconds.

Holography [8] is based on the direct encoding of the phase in the interferences between the object scattered wave field and a reference wave, which is produced by a well-defined secondary object located near the object of interest [9,10]. Several successful demonstrations of x ray FTH have been reported on the imaging of nanostructures [11,12], including the use of a uniformly redundant array as a reference [13]. However, the forward scattering geometry practically restricts the reconstructions to 2D approaches, while in most cases the 3D information is necessary to obtain a complete picture. Furthermore, the high sensitivity of x rays to the displacement fields in a crystal has not been exploited yet. In this context, Bragg coherent diffraction imaging is currently under development for strain imaging in nanocrystals [6]. However, the instability of the inversion algorithms in the presence of inhomogeneous strain fields limits the method to a few well-defined systems, at least for the present time [14]. Strain imaging holography appears as an attractive alternative to these approaches for its capability of providing a direct, robust, and fast 3D reconstruction of the shape, density, and strain field of nanocrystals. In this Letter, we demonstrate the feasibility of displacement field imaging with 3D Bragg Fourier transform holography applied to a SiGe nanocrystal.

Bragg FTH requires that a reference crystal (RC) is placed near the object crystal (OC) to image. The two crystals must have comparable lattice parameters so that the interference of the diffracted wave fields occurs in a high intensity reciprocal space region. If $f_1(\mathbf{r})$ and $f_2(\mathbf{r})$ describe the electron density distribution of the OC and RC, respectively (with $\mathbf{r}$ the direct space vector), then the scattered intensity, in the Fraunhofer approximation for a planar illumination, is

$$I(\mathbf{Q}) \propto |\hat{f}_1(\mathbf{Q}) + \hat{f}_2(\mathbf{Q})|^2, \tag{1}$$

where $\mathbf{Q}$ is the reciprocal space vector and the symbol $\hat{}$ denotes the Fourier transformation. The inverse Fourier transform of the intensity is the sum of four terms:

$$\mathcal{F}^{-1}(I(\mathbf{Q})) \propto \sum_{i,j} f_i(\mathbf{r}) \otimes f_j^{\star}(\mathbf{r}). \tag{2}$$

The two terms that correspond to $i = j$ are the self-convolutions of the OC ($i = 1$) and of the RC ($i = 2$). They are centered around the origin. The third and fourth terms obtained for $i \neq j$ are the object-reference cross convolution and its redundant mirror complex conjugate. They are located around $\mathbf{R}$ and $-\mathbf{R}$, where $\mathbf{R}$ is the reference-object distance. This cross convolution is the holographic image of the OC, and we will refer to it as the object image. Its resolution is given by the size of the RC. Therefore, the size of the object image is the sum of the RC and OC sizes. The use of holography in Bragg

 

geometry allows an easy access to the 3D information because the full 3D intensity pattern can be measured with a sample rotation of a few degrees only [Fig. 1(b)] [15]. Another specificity of the Bragg case is the sensitivity of the hologram to the strain. The strain information is introduced in Eq. (1) as a small perturbation in an effective complex-valued electron density distribution, $f(\mathbf{r}) = \rho(\mathbf{r})\exp[i\phi(\mathbf{r})]$, where $\rho(\mathbf{r})$ is the electron density and $\phi(\mathbf{r})$ is the phase given by the crystal displacement field $\mathbf{u}(\mathbf{r})$ projected onto the Bragg vector [16]. Therefore, the object image is also a complex-valued function, with magnitude and phase. In the following, magnitude will be referred to as density, although the image magnitude may exhibit additional features with respect to the object density, due to, e.g., the convolution process.

The sample used for this work was produced by $e$-beam lithography from a $Si_{1-x}Ge_x$ continuous layer (200 nm thick, $x = 8\%$) grown epitaxially onto a Si $\langle 100 \rangle$ substrate. The OC and RC structures were defined in a positive photoresist with a thickness of 130 nm, using a $SF_6$ reactive ion etching to transfer the pattern into the SiGe layer. The etching depth was chosen in order to remove the SiGe layer outside the OC and the RC, over an area of $100 \times 100\ \mu m^2$. However, as the resist patch was itself partly etched for very small structures, it resulted in a rounding of the original design pattern, as well as a thinning of the RC. Finally, further cleaning of the surface in the vicinity of the structures has been performed by ion beam milling with a very small dose. During this step, amorphization of a thin top layer of the SiGe structure could not be avoided, resulting in a thinner crystalline part than the outer dimension. Scanning electron microscopy (SEM) and atomic force microscopy (AFM) measurements were performed to characterize the two structures of the holographic sample. These measurements exhibit some discrepancies due to charge effect in SEM and limited resolution from the AFM tip [Fig. 1(a)]. However, the nanostructure outer dimensions (length × width × thickness) were estimated to $570 \times 310 \times 190\ nm^3$ for the OC and $180 \times 130 \times 100\ nm^3$ for the RC. The distance $|\mathbf{R}|$ between the two crystals is about 470 nm.

The experiment was carried out at the ID01 beam line (ESRF). The monochromatic beam (wavelength $\lambda = 0.154$ nm) was delivered by a Si-111 monochromator (energy bandwidth of about $1.4 \times 10^{-4}$), resulting in a longitudinal coherence length of about 1 $\mu$m. To increase the flux on the sample, a coherently illuminated Fresnel zone plate made of Au was placed 129 mm upstream [17]. Further details on the focusing setup are given in [18]. The measured size of the focused beam (full width at half maximum) was about 350 and 400 nm in the vertical and horizontal directions, respectively. The transverse coherence lengths were larger than the sample dimension [18] and the longitudinal coherence length was larger than the optical path length difference for the chosen Bragg reflection. The sample was placed horizontally, the beam direction being perpendicular to the object-reference axis [Fig. 1(a)]. The intensity acquisition was performed with a pixel detector (Maxipix, $256 \times 256$ pixels of $55 \times 55\ \mu m^2$ size [19]) mounted 0.93 m downstream.

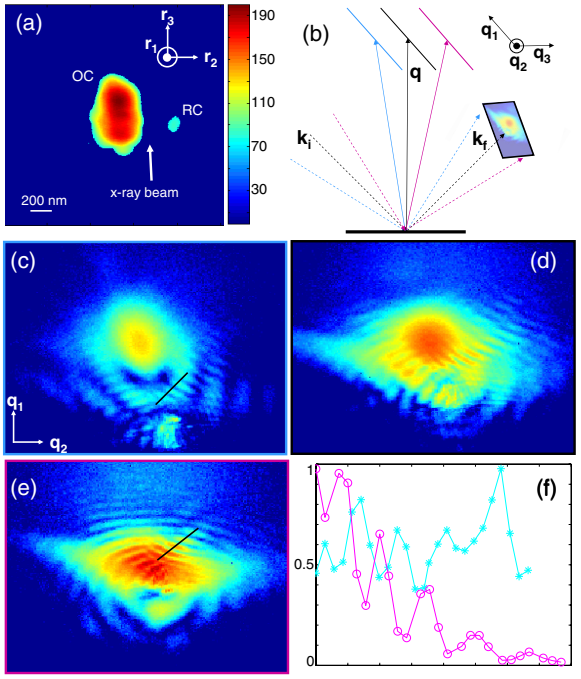


FIG. 1 (color online). (a) AFM characterization of the holographic sample (the arrow indicates the beam direction, the height is given in nm). (b) Sketch of the 3D acquisition in Bragg geometry. (c)–(e) 2D intensity slices taken for different values of $\mathbf{q}_3$. (f) Normalized intensity line cuts extracted along the black lines from (c) (blue stars) and (e) (pink circles).

The coherently scattered intensity is measured around the SiGe (004) Bragg peak (Bragg angle $\theta = 34.5°$) as a function of the wave vector transfer $\mathbf{Q} = \mathbf{k}_f - \mathbf{k}_i$, where $\mathbf{k}_i$ ($\mathbf{k}_f$) is the incident (diffracted) wave vector (with $k_{i,f} = 2\pi/\lambda$). Close to the (004) reflection (Bragg vector $\mathbf{G}_{004}$), the measured reciprocal space positions are given by $\mathbf{q} = \mathbf{Q} - \mathbf{G}_{004}$, with the components $\mathbf{q}_{1,2}$ lying in the detector plane, vertically and horizontally, respectively [Fig. 1(b)]. The $\mathbf{q}_3$ direction, which is probed by scanning the incident angle in steps of 0.01° over an angular range of 0.2°, is perpendicular to $\mathbf{G}_{004}$. These experimental conditions result in a voxel size of $2.4 \times 2 \times 8 \times (10^{-3})^3\ nm^{-3}$. Intensity patterns, obtained for three different values of $\mathbf{q}_3$, are shown in Figs. 1(c)–1(e). The lattice mismatch between the SiGe layer and the Si substrate is about $6 \times 10^{-3}$, large enough to separate the SiGe 3D pattern from the Si Bragg peak. The observed short and high frequency fringes result from finite size effects of the two crystals. Most importantly, strong fluctuations of intensity values observed in the regions where the two systems of fringes overlap [see Fig. 1(c)] demonstrate the coherent interference between the two crystals. The nonuniform fringe contrast that reaches up to 65% in some regions of the reciprocal space [Fig. 1(f)] results from interference effects between two different strain states in the OC and RC,

as it will be further shown in the reconstruction. The 21 slices obtained for different $\mathbf{q}_3$ are stacked into a 3D matrix ($256 \times 256 \times 21$ voxels) for the inversion process.

The direct space image is straightforwardly obtained by a single inverse Fourier transform of the complete 3D intensity matrix. It is transferred to an orthogonal space whose base vectors $\mathbf{r}_{1,2,3}$ are, respectively, perpendicular to the surface, parallel and perpendicular to the OC-RC axis [Fig. 1(a)]. Figure 2 shows the central slice extracted from the complete 3D inverted direct space matrix. In addition to the strong signal of the self-convolution functions in the center, we observe two side maxima, which are the expected object images separated by a distance of about 960 nm, in good agreement with the AFM of Fig. 1(a), where $2|\mathbf{R}| = 940$ nm. Additional background and parasitic signals are observed in the vicinity of the object images. They originate from surface scattering and/or illumination function structures.

One of the two object images is extracted from the complete 3D matrix. Three-dimensional shape views are shown in Figs. 3(a)–3(c). The dimensions are $520 \times 320 \times 140$ nm$^3$. In order to test the image quality, we calculate the object-reference convolution function from the AFM measurement. We compare it to the external shape of the object image (enlarged by 30%) [Fig. 3(d)]. We observe a good agreement in shape. The differences concerning the size are ascribed to the different natures of the imaging techniques: the resolution limited AFM being only sensitive to the external morphology of the sample and the Bragg FTH to its 3D crystalline part. The reduced thickness [140 nm instead of the 290 nm nominal thickness (convolution of the OC and RC thicknesses)] is easily explained by the ion beam milling treatment, which is known to decrease the OC and RC effective crystal thicknesses (by about 50 nm).

The density of the object image is shown in Fig. 4(a), as a stack of 2D slices extracted from the complete 3D reconstruction. The density increase in the center of each slice is a result of a convolution process between the OC and the RC, even if the actual densities of the objects are constant. More interesting in regard to the strain is the phase distribution [shown in Fig. 4(b), corrected from refraction effects]. The difference with the magnitude is evident: the phase is approximately constant throughout the sample, as expected from the convolution of two identically strained crystals. A detailed analysis of the mean phase value (calculated over $\mathbf{r}_1$ and $\mathbf{r}_2$) as a function of the $\mathbf{r}_3$ coordinate, i.e., parallel to the OC length, shows a linear increase followed by a plateau (300 nm wide) and another similar linear increase [Fig. 4(c)]. This phase behavior is obtained after carefully centering the OC Bragg peak in the 3D intensity matrix in order to minimize the total phase shift. The complete phase shift behavior is fully reproduced if one assumes that the OC electron density $f_1(r_3)$ is constant inside the crystal, while for the RC, $f_2(r_3)$ is proportional to $\exp(iar_3)$. An agreement between the experiment and the model is obtained for $a = 0.012$ nm$^{-1}$, allowing us to fit the RC and the OC lengths, equal to 140 and 400 nm, respectively [solid line in Fig. 4(c)]. The origin of a linear phase as a function of $r_3$ can be explained if the RC lattice planes are not parallel but slightly inclined with respect to the OC. This leads to a linear displacement $\mathbf{u}_{004}$ of the OC atomic positions as a function of $r_3$ [see bottom inset of Fig. 4(c)]. The displacement is given by $u_{004} = \frac{a}{G} r_3 = 2.6 \times 10^{-4} \times r_3$, which corresponds to a small tilt ($\alpha$) of about 0.02°, easily explained by relaxation effects in the nanocrystals [20]. Furthermore, phase variations (of about 1 rad) are observed, systematically accompanied by a decrease of the image density. This is a typical signature of inhomogeneous strain fields, arising from relaxation effects in the patterned crystals. These effects are more visible at the image surface and interface, as expected.

Therefore, we demonstrate here the principle of Bragg FTH, which allows the electron density and the displacement field to be directly determined in 3D. This method

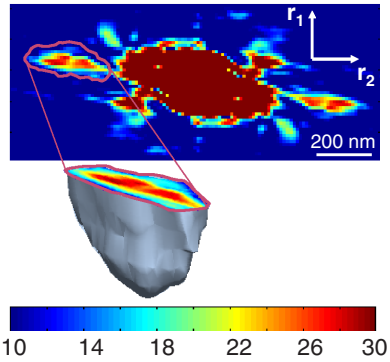


FIG. 2 (color online). 2D slice taken in the center of the 3D direct space matrix obtained by inverse Fourier transforming the 3D intensity matrix. One of the two object images is emphasized by a pink line (inset: the same image in its 3D representation).

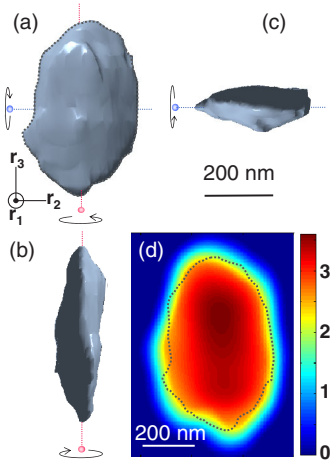


FIG. 3 (color online). (a)–(c) 3D isosurface views of the object image density. (d) 2D convolution of OC with RC obtained from the AFM measurements (Fig. 1); the black dotted line is the enlarged contour plot obtained from the 3D view shown in (a).

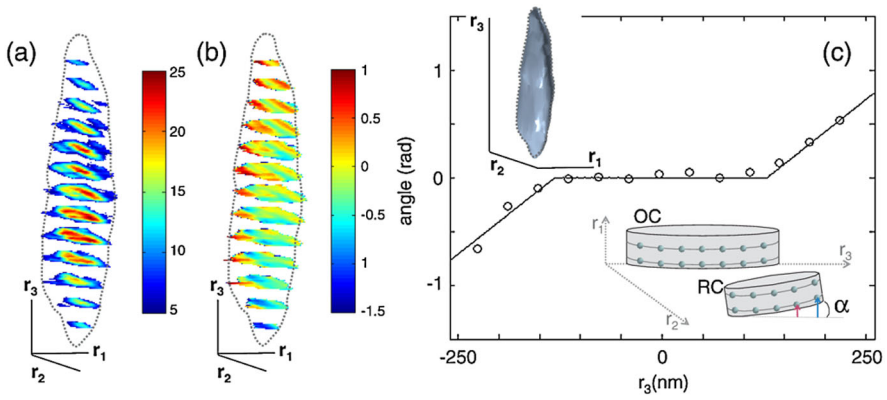


FIG. 4 (color online). Stack of 2D slices extracted from the 3D direct space matrix. (a) Internal view of the object image density [the color scale is linear (arbitrary unit)] and (b) phase (the angular color scale is given in radians). (c) Mean values of the object image phases (black circles) as a function of $r_3$ (in nm), calculated from (b); expected phase behavior (solid line) calculated for a RC density function with linear phase shift. This phase behavior results from a tilt ($\alpha$) of the RC lattice planes with respect to OC. The inset at the bottom shows two values of $\mathbf{u}_{004}$ (pink and blue arrows), which increases linearly with $\mathbf{r}_3$ when the RC is tilted.

overcomes the convergence problems of lensless imaging iterative algorithms. This issue is particularly difficult to solve for inhomogeneous strain fields, as it relies on *a priori* knowledge [14]. Hence, the Bragg FTH method will be a unique tool to study elastic and plastic properties of nanomaterials, such as the strain field developed in the vicinity of a dislocation or during an external mechanical or piezoelectrical stress. In the following, we finally discuss the application limits of our method.

The possibility to measure the hologram relies on the visibility of the interferences between the OC and RC scattered wave fields. Therefore, the two wave fields have to overlap in a high intensity reciprocal space region, i.e., near the OC Bragg peak. For homogeneously strained nanocrystals, the overlapping is typically ensured for maximum mean lattice mismatch value $\Delta a/a$ of about $2\pi/|\mathbf{G}|T$, where $T$ is the RC dimension in the direction of $\mathbf{G}$. The presence of an inhomogeneous strain field in the OC will lead to an additional broadening of the OC peak. The maximum allowed $\Delta a/a$ will increase as $2\pi/|\mathbf{G}|T + \Delta a'/a$, where $\Delta a'/a$ is the inhomogeneous component of the strain field in the OC. Therefore, the presence of inhomogeneous strain fields will further preserve the hologram, allowing for a lensless imaging technique in a strain domain which is difficult to address with other phase retrieval microscopy methods. The spatial resolution of the object image imposed by the reference crystal is expected to improve in the near future, due to the increase of the coherent flux provided by better x-ray focusing optics or by the x-ray free electron laser.

To conclude, we have demonstrated the 3D imaging of a nanocrystal with Bragg FTH. In addition to the shape, we obtained an internal view of the density and displacement field. The simplicity and robustness of the inversion paves the way to *in situ* investigations of inhomogeneous strain fields in a nanocrystal. We believe that this technique will bring new insight to understand current strain related problems in nanomaterial research.

We acknowledge the ID01 staff (ESRF) for technical support, O. Bikondoa, F. Mastropietro, and A. Sentenac for fruitful discussions, and S. Le Denmat for the AFM characterizations. This work was funded by the ANR (ANR-08-JCJC-0095-01), the FWF Vienna (SFB025), and the PLATON project of the Austrian Nanoinitiative.

*virginie.chamard@univ-cezanne.fr
†Now at: PSI, CH-5232 Villigen, Switzerland.
‡Now at: Synchrotron Soleil, L'Orme des Merisiers Saint-Aubin BP 48, 91192 Gif-sur-Yvette, France.

[1] A. Guinier and D. L. Dexter, *X-Ray Studies of Material* (Interscience, New York, 1963).
[2] C. Lamberti, Surf. Sci. Rep. **53**, 1 (2004).
[3] M. M. Roberts *et al.*, Nature Mater. **5**, 388 (2006).
[4] R. W. Gerchberg and W. O. Saxton, Optik **35**, 237 (1972).
[5] J. Miao *et al.*, Nature (London) **400**, 342 (1999).
[6] M. A. Pfeifer *et al.*, Nature (London) **442**, 63 (2006).
[7] B. Abbey *et al.*, Nature Phys. **4**, 394 (2008).
[8] D. Gabor, W. E. Kock, and G. W. Stroke, Science **173**, 11 (1971).
[9] G. W. Stroke and D. Falconer, Phys. Lett. **13**, 306 (1964).
[10] J. T. Winthrop and C. R. Worthington, Phys. Lett. **15**, 124 (1965).
[11] S. Eisebitt *et al.*, Nature (London) **432**, 885 (2004).
[12] L.-M. Stadler *et al.*, Phys. Rev. Lett. **100**, 245503 (2008).
[13] S. Marchesini *et al.*, Nat. Photon. **2**, 560 (2008).
[14] A. A. Minkevich *et al.*, Phys. Rev. B **76**, 104106 (2007).
[15] G. J. Williams *et al.*, Phys. Rev. Lett. **90**, 175501 (2003).
[16] S. Takagi, J. Phys. Soc. Jpn. **26**, 1239 (1969).
[17] K. Jefimovs *et al.*, Microelectron. Eng. **84**, 1467 (2007).
[18] A. Diaz *et al.*, Phys. Rev. B **79**, 125324 (2009).
[19] C. Ponchut *et al.*, Nucl. Instrum. Methods Phys. Res., Sect. A **576**, 109 (2007).
[20] We note that a local wave front curvature of the illumination, with a wave vector inclined by $\alpha$, would have *exactly* the same signature.